PERGAMON

International Journal of Heat and Mass Transfer 43 (2000) 1537–1546

International Journal of HEAT and MASS TRANSFER

www.elsevier.com/locate/ijhmt

Mixed convection in radial flow between horizontal plates — II. Experiments

Helmar Van Santen, Chris R. Kleijn*, Harry E. A. Van Den Akker

Kramers Laboratorium voor Fysische Technologie, Delft University of Technology, Prins Bernhardlaan 6, 2628 BW Delft, Netherlands

Received 13 November 1998; received in revised form 16 July 1999

Abstract

Mixed convection of a forced radially outward flow with secondary, buoyancy induced convection has been studied experimentally in an axisymmetric geometry, consisting of two differentially heated, horizontal, coaxial, circular plates with a diameter of 50 cm and a mutual distance of 2 cm. Through the centre of the upper plate, a laminar forced air flow is supplied. Particle image velocimetry, flow visualisation and local temperature measurements have been used to study the onset of thermal instability as a function of the inflow and temperature difference, and to validate the numerical results obtained in Part I of this paper. © 2000 Elsevier Science Ltd. All rights reserved.

1. Introduction

Buoyancy driven secondary convection in a forced laminar flow may lead to heat transfer enhancement and the onset of turbulence. The understanding of thermal and flow characteristics in mixed convection is of practical importance, e.g. in the design of compact heat exchangers and chemical vapor deposition reactors, or in the cooling of micro-electronic equipment. In the present paper, mixed convection is studied experimentally in an axisymmetric geometry, consisting of two differentially heated circular, co-axial horizontal plates with a forced, initially axial, then radially outward laminar flow (see Fig. 1). The relevance of this geometry is discussed more elaborately in Part I, i.e. the numerical part, of this paper [1].

In Part I, it was found that the interaction of the forced flow and the secondary, buoyancy induced convection may lead to transversal, axisymmetric, torus-shaped rolls and/or three-dimensional roll patterns. For gases, with a Prandtl number of 0.7, the forced flow at small radial distances causes the buoyancy induced secondary flows to be torus-shaped rolls. At larger radial distances, these rolls break up and form a more irregular, three-dimensional pattern, similar to merely buoyancy induced convection between two differentially heated horizontal plates. The transition between these two regions depends on the Reynolds and Rayleigh numbers. In this part of the paper, experiments are presented to validate these numerical results.

A range of experimental techniques have been successfully applied in mixed convection flows e.g. in a plain Poiseuille flow with a vertical temperature gradient, in order to measure different aspects of the flow. Whole field methods such as visualisation studies and laser interferometric measuring techniques, have been applied to determine the presence of longitudinal and/or transversal rolls and their spatial structure [2–5].

* Corresponding author. Tel.: +31-15-278-2835; fax: +31-15-278-2838.

E-mail address: crkleijn@klft.tn.tudelft.nl (C.R. Kleijn).

0017-9310/00/$ - see front matter
PII: S0017-9310(99)00233-1

Nomenclature

a	Thermal diffusivity (m^2/s)
d_e	Diameter seeding particles (m)
d_I	Diameter interrogation area (m)
g	Acceleration of gravity (m/s^2)
H	Distance between the plates (m)
M	Magnification
Ra	Rayleigh number
Re	Reynolds number
r	Radical coordinate (m)
r_{crit}	Radius where buoyancy induced flows emerge (m)
$r_{crit,long}$	Radius where longitudinal rolls may emerge (m)
$r_{crit,trans}$	Radius where transversal rolls may emerge (m)
ΔT	Temperature difference (K)
Δt	Time separation (s)
Δu	Velocity variation (m/s)
v_r	Radial velocity (m/s)
z	Axial coordinate (m)
α	Thermal expansion coefficient (1/K)
Φv	Volumetric flow rate (m^3/s)
ν	Kinematic viscosity (m^2/s)
σ	Standard deviation

The temporal behaviour has been determined with more local measurement techniques, such as internal temperature probe measurements and laser Doppler anemometry [4,6,7]. The main purpose of the present study is to validate the numerical results obtained in Part I. Therefore both the spatial and the temporal properties of the flow have been measured in the geometry of Fig. 1. For determining the spatial properties of the flow field, the quantitative field measurement technique particle image velocimetry (PIV) has been used, as well as more qualitative flow visualisations. In addition, local, instantaneous temperature measurements were performed to obtain information on characteristic time scales in the flow.

2. Experimetal set-up

In Fig. 2 a schematic of the experimental set-up is shown. The fluid is supplied as a fully developed, laminar, isothermal Poiseuille flow from a long, straight tube, through a 2-cm diameter hole in the top plate. The operating fluid is air at atmospheric pressure and at the temperature of the cold upper plate (close to room temperature). In the absence of buoyancy effects, the velocity field, after an entrance region and terms of order $1/r^3$ being ignored, corresponds to a Poiseuille profile, with the average velocity decreasing inversely proportional to the radial distance coordinate r:

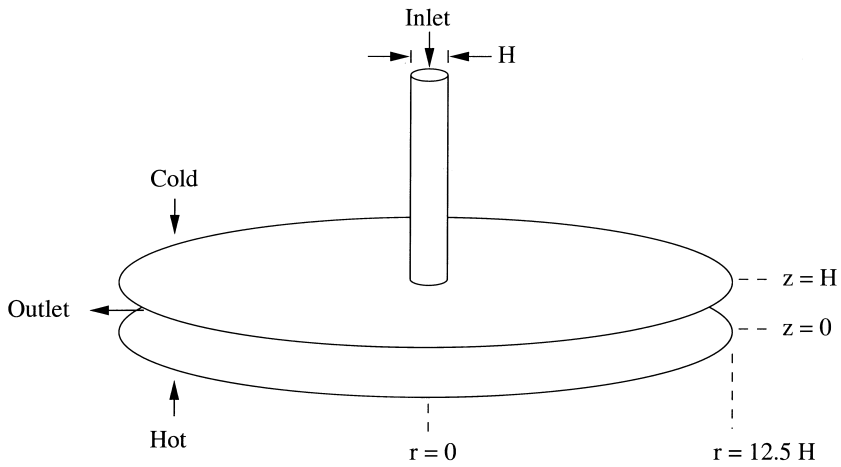

Fig. 1. Schematic of the geometry.

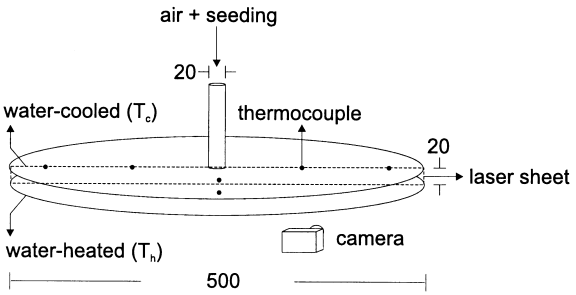

Fig. 2. Schematic of the experimental set-up (measures in millimetres).

$$v_r(r,z) = \frac{1}{r}\frac{3\Phi_v}{\pi H^3} z(H-z) \tag{1}$$

with $v_r(r,z)$ the velocity in the r-direction, H the spacing of the plates, and Φ_v the volume flow. The characteristic velocity for forced convection thus is a function of the radial position. In order to characterise the flow uniquely, a single characteristic velocity has to be selected. In this paper, this is selected as $v_r(H,\frac{1}{2}H)$ in Eq. (1). The characteristic length scale is selected as the distance between the plates. A flow rate of 1.27×10^{-4} m^3/s corresponds to $Re = 100$.

The top and bottom plates have been made from 2 cm thick aluminium, and are water cooled and heated, respectively. A labyrinth has been milled in each plate, through which the cooling and heating water flows. The temperature uniformity across the plates was monitored with PT-100 thermistors and was better than 0.02 K (2σ). A temperature difference of 6.2 K between the plates corresponds to a Rayleigh number, $Ra = gH^3\alpha\Delta T/av$, of approximately 5000.

The geometry studied is very sensitive to disturbances originating from the surroundings because of the relatively large outflow boundary. Therefore, the set-up was placed within a containment, kept at very slight overpressure. Furthermore, the temperatures of the plates were selected symmetrically around the temperature of the surroundings, usually about 293 K.

For the visualisation and PIV velocity measurements, the air flow was seeded with smoke particles, generated by the ZR20 Mk2 fog generator [8] by heating a mixture of triethylene glycol and propane 2-diol in water. The resulting smoke droplets had an average diameter of 1.2 μm, with a standard deviation of 0.2 μm.

The smoke particles were periodically illuminated with a vertical pulsating laser sheet, simulated with a sweeping laserbeam. The set-up that was used to generate the sweeping beam is schematically shown in Fig. 3. The beam of a 4 W Ar^+ laser was focussed on the turning point of a Galvano meter. This point in turn was the focal point of a converging lens. The two lenses were selected in order to have a parallel laser thinner than 0.8 mm ($1/e^2$) throughout the experimental set-up. The Galvano meter was steered with a sawtooth signal. This means that only the upward sweeps were detected. The sweep back of the mirror was sufficiently fast in order to be invisible on the photographs. Sweep frequencies were typically between 20 and 50 Hz for the PIV measurements, and 100 Hz for the visualisation experiments.

In addition to the visualisation and PIV experiments, local instantaneous temperature measurements were performed to obtain information on characteristic time scales in the flow. For this purpose, a probe was used, consisting of a 4-mm U-shaped, 20-μm diameter spirally-shaped Tungsten wire. The response time was below 0.1 s, sufficiently low to capture all relevant frequencies.

3. Particle image velocimetry

Particle image velocimetry (PIV) is a measuring technique for the instantaneous measurement of a spatially resolved velocity field. It belongs to the class of pulsed-light velocimetry techniques where the flow is seeded with small, passive tracer particles. These particles are illuminated at fixed time intervals. From the displacement between the successive illuminations, the local velocity is derived. In particle image velocimetry, the velocity field is resolved at fixed points, where the local velocity is determined from the average displacement(s) of 10–20 tracer particles in an interrogation volume around this point. Detailed information can be found in Refs. [9–11].

For a correct estimate of a local velocity with PIV, the velocity in the interrogation area must be uniform. The secondary, buoyancy induced recirculations in the flow studied, result in large gradients that may cause errors in the estimated velocity. This error can be separated into two parts: (i) detection bias, i.e. the height of the displacement peak decreases as a result of differ-

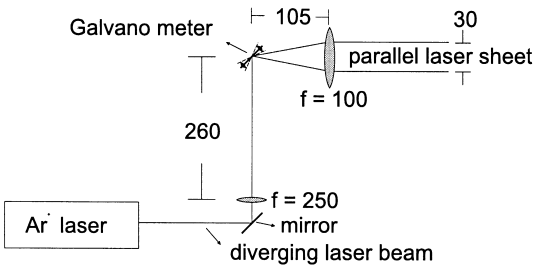

Fig. 3. Schematic of the experimental set-up to simulate a parallel pulsating laser sheet (measures in millimetres).

ent velocities present, and (ii) gradient bias, i.e. the magnitude of the velocity is systematically underestimated as the chance of a particle disappearing from the interrogation area before the second illumination is larger for fast moving particles. Thus, the PIV system parameters have to be selected in order to keep the resulting errors sufficiently small. Adrian [9] shows that:

$$\frac{M|\Delta u|\Delta t}{d_e} < 1 \tag{2}$$

for a detection chance of 92%, where M is the magnification, d_e the diameter of the seeding particles in the recording, Δu the velocity variation within an interrogation area, and Δt is the time separation. In addition,

$$\frac{M|\Delta u|\Delta t}{d_I} < 1 \tag{3}$$

for a systematic error of less than 5%, where d_I is the diameter of the interrogation area in the recording plane. The numerical results presented in Part I [1], indicate that:

$$\frac{M\Delta u}{d_I} < 2.5 \times 10^{-3}\ \mathrm{s}^{-1} \tag{4}$$

In order to obey the above criteria, the PIV system parameters have been selected as: $d_e = 20$ μm, $M = \frac{1}{3}$, $d_I = 0.6$ mm, $\Delta t < 0.05$ s.

No preshift is applied in the PIV measurements, while the two illuminations are recorded on the same material. Drawbacks are that there is a 180° directional ambiguity in the velocity and that velocities which are low compared to the maximum velocity, easily lead to erroneous vectors. The directional ambiguity, however, can be solved because the direction of rotation of the recirculations can be derived from the direction of the forced flow. Furthermore, the errors at low velocities are not large enough to warrant the problems and errors that accompany preshifting techniques.

The flow fields are recorded on photographic film with a standard 35-mm camera. For the PIV measurements, the magnification was $M = \frac{1}{3}$, rendering images in the flow of 10 cm in horizontal direction and 2 cm in vertical direction, the latter being determined by the distance between the plates. The film is developed and then scanned with a resolution of 2820 dpi optical with the Minolta QuickScan35 diascanner [12]. Thus, the interrogation areas of 2×2 mm^2 in the flow are scanned with a resolution of approximately 64×64 pixels. The quality of the digitisation is illustrated in Fig. 4, where a part of the photo negative through a microscope is compared to a diascan of the same part. The figure shows, that the resolution of the scanner is sufficient compared to that of the selected film. Furthermore, the figure shows that particles indeed are recorded with a diameter of 20 μm, as used in Section 3. For the visualisation experiments, the magnification M was $\frac{1}{6}$, to image a larger part of the flow.

A representative example of the PIV measurements of a buoyancy induced roll is shown in Fig. 5. For the data processing, the program PIVWARE by Westerweel is used [11]. In PIVWARE, the cross-correlation is calculated via FFTs and a Gaussian distribution function is used to determine the location of the maximum of the displacement peak with subpixel accuracy.

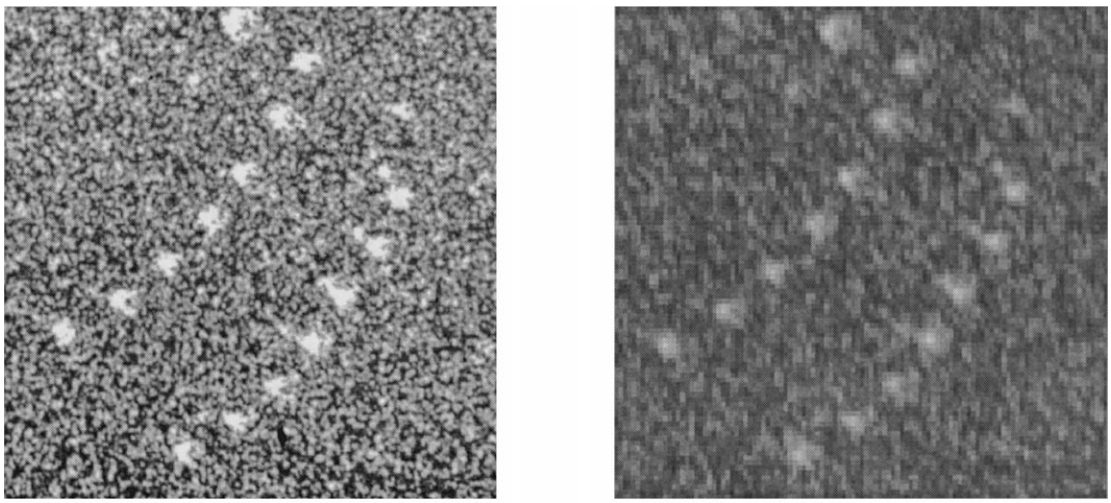

(a) (b)

Fig. 4. Comparison photo-negative and digitisation. (a) Microscope picture; (b) diascanner.

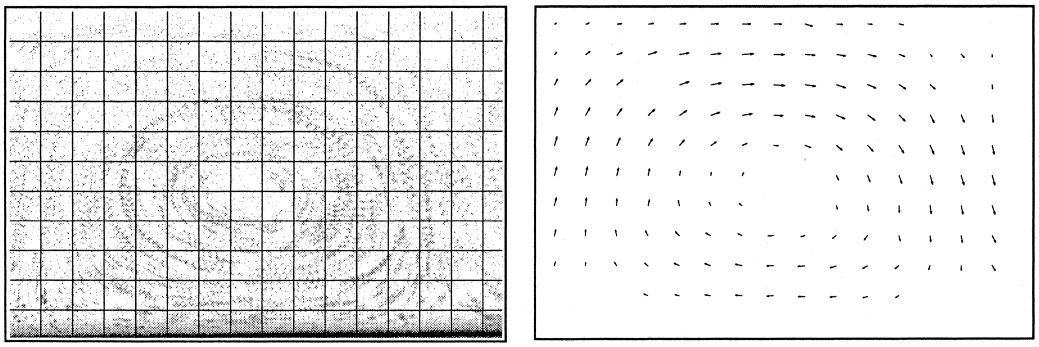

Fig. 5. Illustration of the PIV measurements in buoyancy induced flows. (a) Digitised photo negative with interrogation areas; (b) reconstructed velocity field.

The figure illustrates that the velocity field can be reconstructed well. The velocity near to the centre of the roll cannot be determined, because the velocity and seeding concentration are too low. In addition, it is hard to reconstruct the velocities close to the lower and upper boundaries, because of reflections and low velocities.

4. Experimental results

Three measuring techniques were applied to study the mixed convection flow and to validate the numerical results presented in Part I of this paper [1]: (i) flow visualisation, to obtain a qualitative picture of the flow and to determine the radial coordinate for the onset of thermal instability, (ii) PIV, for quantitative velocity measurements that can be compared to simulations, and (iii) local temperature measurements, to obtain information on characteristic time scales in the flow. The results are presented below.

4.1. Visualisations

In Fig. 6a, a representative picture of the visualised

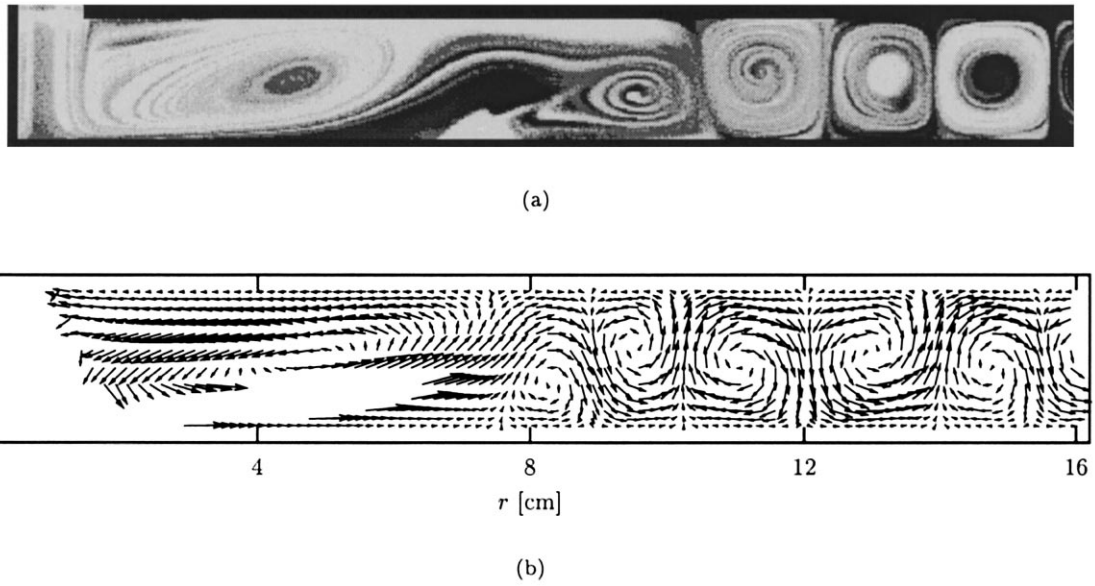

Fig. 6. Comparison between visualisation and simulation at $Re = 40$, $Ra = 3800$ and $Pr = 0.7$. In the simulated flow field, the velocity vectors with a large magnitude have been left out for presentational purposes. (a) Visualised flow field; (b) simulated velocity field.

flow field is shown for an inflow and temperature difference corresponding to $Re = 40$ and $Ra = 3800$. The vertical laser sheet is directed through the centre of the plates. The seeded air flows in through the top left of the figure and flows radially outwards to the right. The flow is transient, so Fig. 6a is an instantaneous recording of the flow in the plane of the sheet.

The first recirculation with centre at $r \approx 4$ cm is induced by the inflow. This recirculation is steady, axisymmetric, torus-shaped and almost independent of the temperature difference between the plates. At these Rayleigh and Reynolds numbers, the secondary, buoyancy induced flows start immediately after this forced convection induced recirculation. At larger radial distances, the effect of the forced flow diminishes, and free convection becomes the dominating effect.

As a comparison, the projection on the r–z plane of the simulated velocity field in the same part of the geometry is shown for the same dimensionless operating conditions (see Fig. 6b). The location of the centre and the size of the steady forced convection induced recirculation near to the inlet are the same for the experiment and the simulation. Other aspects can be compared only qualitatively, as the flow is transient. Good agreement, however, can be seen in shape and size of the buoyancy induced recirculations. Furthermore, as in the visualisation, the effect of the forced flow is almost invisible at larger radial distances.

The projections of the simulated and experimental flow field suggest that the buoyancy induced recirculations are axisymmetric. Everywhere but close to the inlet, however, the flow field is actually fully three-dimensional. This is illustrated in Fig. 7, where a contour plot is shown of the simulated z-velocities in a horizontal plane at $z = \frac{1}{2}$, at the same instant as the velocity plot in Fig. 6b. The recirculations near to the inlet exhibit some form of axisymmetry, but a more chaotic pattern is observed at larger radial distances. This is also observed in the experiments, e.g. in video recordings of the flow, where the concentration of seeding particles in a recirculation varies in time, while radial position and size hardly change.

Flow visualisation also gives quantitative results for the radial coordinate r_{crit} where the steady forced flow becomes unstable and buoyancy induced flows emerge. The mechanisms that determine r_{crit} are complicated. When r_{crit} is small, the secondary flow resulting from this instability consists of more or less axisymmetric transversal rolls (rolls with their axis of rotation perpendicular to the forced flow). When r_{crit} is larger, the secondary flow consists of more irregular, three-dimensional rolls. For transversal rolls, critical Rayleigh and Reynolds numbers are available in literature for Cartesian geometries. At a fixed Rayleigh number, there is a maximum Reynolds number up to which transversal rolls may occur. In the geometry studied, the effective Reynolds number decreases with r. Therefore, at a fixed Rayleigh and inlet Reynolds number, a critical radius exists where transversal rolls may occur, $r_{crit,trans}$. In first order approximation, $r_{crit,trans}$ depends linearly on the Reynolds number. For the three-dimensional rolls, no similar relation can be derived. It can, however, be expected that the instability leading to this type of rolls is less sensitive to the Reynolds number as these rolls can be related to longitudinal rolls and the critical Rayleigh number for longitudinal rolls is independent of the Reynolds number. These mechanisms are discussed more elaborately in Part I of this paper [1].

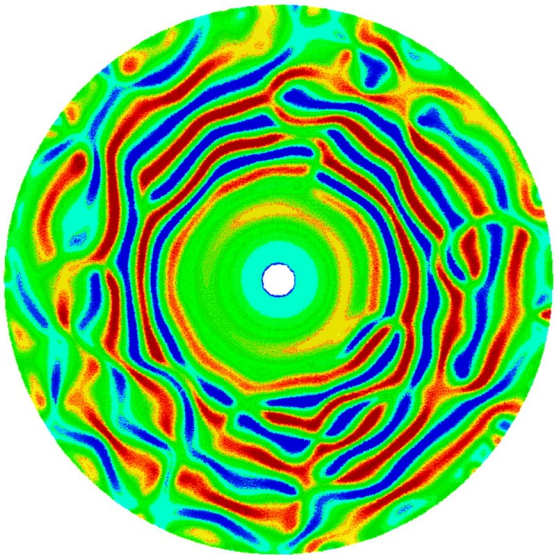

Fig. 7. Three-dimensional flow at $Re = 40$ and $Ra = 3800$. Contour plot of the instantaneous z-velocities in a cross section at $z = 1/2$.

In Fig. 8 the experimentally observed r_{crit} is compared to the simulated r_{crit} at different values for Re. Rayleigh is kept constant at $Ra = 2900$. The experimental results at large Reynolds numbers may be inaccurate, because the outlet boundary has some effect. Furthermore, at low Reynolds numbers, it is difficult to distinguish between the onset of thermal instability and the forced convection induced recirculation near to the inlet. The values and trends in the experiments and simulations, however, are in good agreement.

For $Re \lessapprox 50$, the buoyancy induced flow found at r_{crit} consists of transversal rolls. The r_{crit} found, however, is approximately a factor four larger than $r_{crit,trans}$ that is predicted by linear stability theory for transversal rolls in rectangular geometries [13]. This is probably due to the visual criterion for thermal instability.

In the experiment, only the larger instabilities can be observed. In the time required for a small instability to become sufficiently large to be detected, it is transported radially outward by the forced flow, resulting in an over-estimation of r_{crit}. For $Re \gtrapprox 50$, r_{crit} is found to increase sublinearly only with the Reynolds number, whereas a linear dependency is expected when transversal rolls are the only instability. The resulting buoyancy induced flow, however, consists of more chaotic, three-dimensional rolls. As expected, r_{crit} for this type of rolls is less sensitive to the Reynolds number.

4.2. PIV measurements

Quantitative measurements on the spatial distribution of the velocities have been obtained by particle image velocimetry. In Fig. 9, two reconstructed velocity fields are plotted at the same Rayleigh number, 2900, but at two different Reynolds numbers, 20 and 50 for Fig. 9a and b, respectively. Though lower than the r- and z-velocities, the θ-velocities are nonzero. Therefore, the flow fields in Fig. 9 are the two-dimensional projections of the actual velocities in an rz-plane. Velocity vectors with a low signal to noise ratio have been left out.

At $Re = 20$ (Fig. 9a), the buoyancy secondary flows in the part of the geometry shown have become the dominating effect. In the buoyancy induced rolls, however, the forced flow still is visible through higher velocities in the part of the rolls with positive r-velocities. Furthermore, the centre points of the rolls do not lie on a horizontal line due to the meandering of the forced convection. At $Re = 50$, (Fig. 9b) the critical radial coordinate for thermal instability is in the area plotted. Though at the same Rayleigh number as in Fig. 9a, the higher characteristic velocity of forced flow still largely suppresses vertical motions. The velocities in the emerging buoyancy induced rolls could not be measured. This is due to their relatively low velocity. Furthermore, simulations show that at these conditions, with a large r_{crit}, the secondary flows are three-dimensional. This also may have hampered the PIV measurements in the recirculations.

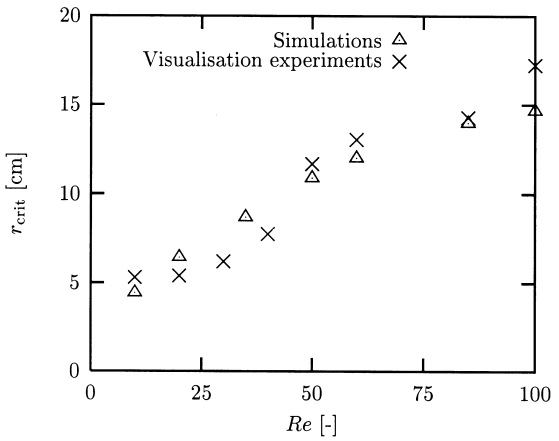

Fig. 8. Radial coordinate where the forced flow becomes unstable at $Ra = 2900$.

Table 1
Comparison experimental and simulated velocities at $Ra = 2900$. The maximum absolute vertical velocity between $r = 16$ and 20 cm is shown for different Reynolds numbers

Re	Experiment (cm/s)	Simulation (cm/s)
10	1.6	1.8
20	1.7	1.9
50	0.5	0.5
100	0.1	0.2

An exact comparison of the experimental and simulated velocity fields can not be made as the flow is transient. With the visualisation results in Fig. 6 it was already shown that the qualitative properties of experiment and simulation are the same. In order to quantitatively compare the velocities, the computed and measured maximum velocity in the vertical z-direction between $r = 16$ cm and $r = 20$ cm for experiment and simulation are listed in Table 1 for several Reynolds numbers and $Ra = 2900$. The results are in good agreement, though experimental values tend to be lower. The reason probably is that PIV tends to underestimate the velocity when gradients are present. The maximum velocities at $Re = 10$ and 20 are approximately the same, as for both cases the secondary flows are settled in the plotted region. At the higher Reynolds numbers, the forced flow is still more important than the secondary flows, suppressing most buoyancy effects.

4.3. Local temperature measurements

Flow visualisation and PIV were applied to study the instantaneous velocity fields. The flow, however, is transient. In order to obtain information on the time scales in the flow, local temperature measurements were performed. A drawback of the applied method is that an intrusive probe is used. This may have affected the measurements as mixed convection flows are very sensitive to geometrical effects. In Fig. 10a the measured local temperatures are shown as a function of time, at two different locations in the geometry, both at $r = 20$ cm but with a difference in angle of π. The two lines were measured at the same

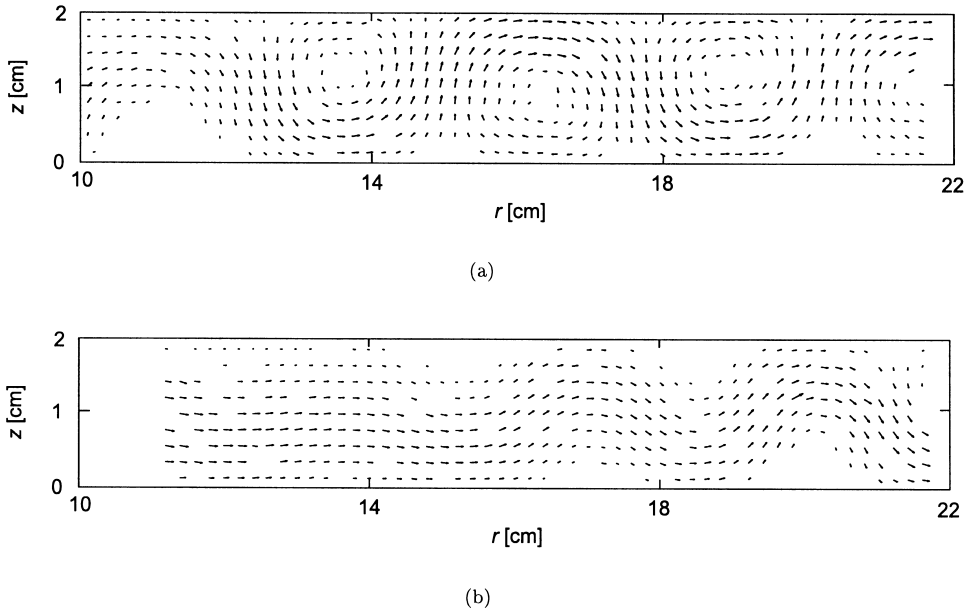

Fig. 9. PIV measurements at $Ra = 2900$. A vector with length 1 cm corresponds to a velocity of 10 cm/s. (a) $Re = 10$; (b) $Re = 50$.

moment in time, while the gas flow and temperature difference correspond to $Re = 40$ and $Ra = 3500$. As a comparison, in Fig. 10b the simulated local temperatures are shown at the same location and conditions.

In both the experiment and the simulation, there is little correlation between the two signals, even though they are at an axisymmetric location with the same radial position. This illustrates that, at the position where the temperature is monitored, the flow is nonaxisymmetric. The effective Reynolds number at $r = 20$ cm has reduced to 4. Furthermore, the curvature of the forced flow at this radial position is small. Therefore, the forced flow at this location is not sufficiently strong to modulate the free convection in some form of axisymmetry. This forced flow, however, still has the effect of transporting the secondary flows radially outward at a more or less constant rate. The frequency that follows from the two figures corresponds to a velocity of the flow structures of the order of the mean forced radial flow at this position. (Actually, in the experiments it is slightly higher, and in the simulation slightly lower.) The small difference in frequency between experiment and simulation may be caused by small differences in the operating parameters, or by the effect of the intrusive probe. The amplitude of the experimental temperature variations is lower than that of the simulations, while the experimental signal is smoother. This is caused by the 4-mm size of the probe, which is large compared to the 2-cm distance between the plates.

5. Concluding remarks

In the geometry studied, the axisymmetric forced flow has a substantial effect upon the secondary, non-axisymmetric buoyancy induced convection. Three measuring techniques have been applied to study this mixed convection flow and to validate the results presented in the numerical part of this paper: Flow visualisation, particle image velocimetry and local temperature measurements. The results of the experiments show good qualitative and quantitative agreement with the simulations. In the visualisation experiments, the proposed mechanisms that determine the critical radial distance where the steady forced flow becomes unstable with respect to buoyancy effects, are confirmed. The critical radial distance initially increases linearly with Re, as would be expected for transversal rolls. For higher Reynolds numbers, this dependency weakens and the resulting secondary flows are irregular, three-dimensional rolls. Also, the velocity fields measured with PIV show excellent agreement with those in the simulations. The time-behaviour measured with a local temperature shows the absence of axisymmetry at larger radial distances, as found in the simulations. The small differences in the actual values of the measured frequencies, compared to the simulations can be attributed to the limitations of the experimental technique used.

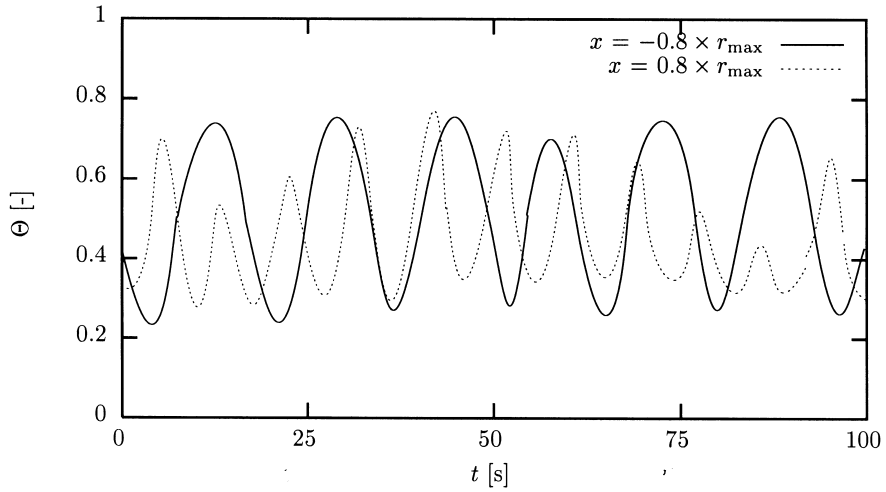

(a)

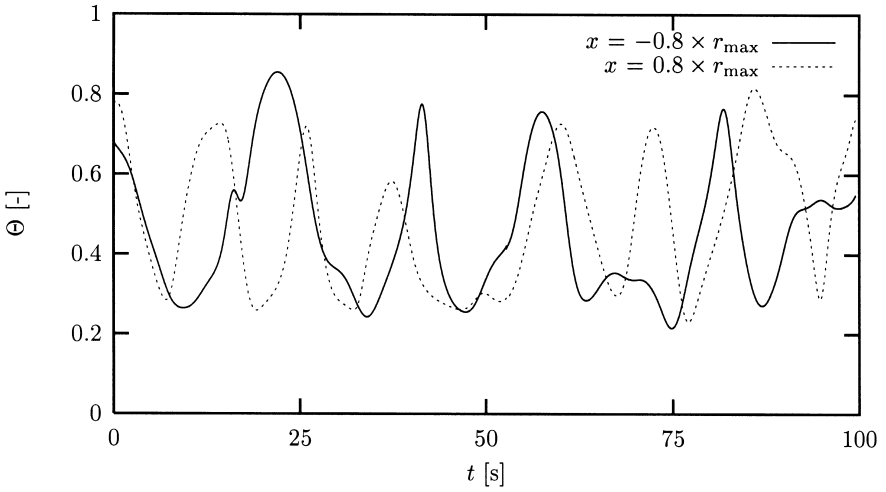

(b)

Fig. 10. Comparison of measured and simulated local temperatures. (a) Experiments; (b) simulation.

Acknowledgements

The authors wish to thank E.M. Van Drielen and H. Van Haagen for their assistance with the experiments and Dr. R.F. Mudde for valuable discussions.

References

[1] H. Van Santen, C.R. Kleijn, H.E.A. Van Den Akker, Mixed convection in radial flow between horizontal plates—I. Numerical simulations, Int. J. Heat Mass Trans. 43 (2000).

[2] C.H. Yu, M.Y. Chang, T.F. Lin, Structures of moving transverse and mixed rolls in mixed convection of air in a horizontal plane channel, Int. J. Heat Mass Trans. 40 (1997) 333–346.

[3] K.C. Cheng, L. Shi, Visualization of convective instability phenomena in the entrance region of a horizontal rectangular channel heated from below and/or cooled from above, Exp. Heat Trans. 7 (1994) 235–248.

[4] J.K. Platten, J.C. Legros, Convection in Liquids, Springer-Verlag, Berlin, 1984.
[5] K.C. Chin, J. Ouazzani, F. Rosenberger, Mixed convection between horizontal plates—II. Fully developed flow, Int. J. Heat Mass Transfer 30 (8) (1987) 1655–1662.
[6] M.T. Ouazzani, J.K. Platten, H.W. Müller, M. Lücke, Etude de la convection mixte entre deux plans horizontaux à températures différentes—III, Int. J. Heat Mass Transfer 38 (1995) 875–886.
[7] E. Schröder, K. Bühler, Three-dimensional convection in rectangular domains with horizontal throughflow, Int. J. Heat Mass Transfer 38 (1995) 1249–1259.
[8] JEM Smoke Company Ltd. http://www.jemsmoke.com. 1998.
[9] R.J. Adrian, Particle-imaging techniques for experimental fluid mechanics, Ann. Rev. Fluid Mech. 23 (1991) 261–304.
[10] R.D. Keane, R.J. Adrian, Optimization of particle image velocimeters, Part 1: double pulsed systems, Meas. Sci. Technol. I 1 (1990) 1202–1215.
[11] P.M. Westerweel. Digital particle image velocimetry. Ph.D. thesis, Delft University of Technology, 1993.
[12] Minolta. http://ows.minoltausa.com/minolta/owa/productlist.list?line = sa. 1998.
[13] K. Muralidhar, F.A. Kulacki, Stability of mixed convection flow, Heat and Fluid Flow 8 (1987) 228–234.